Physical Modeling of Spiral Inductors on Silicon

C. Patrick Yue, *Member, IEEE,* and S. Simon Wong, *Fellow, IEEE*

Abstract—This paper presents a physical model for planar spiral inductors on silicon, which accounts for eddy current effect in the conductor, crossover capacitance between the spiral and center-tap, capacitance between the spiral and substrate, substrate ohmic loss, and substrate capacitance. The model has been confirmed with measured results of inductors having a wide range of layout and process parameters. This scalable inductor model enables the prediction and optimization of inductor performance.

Index Terms—Eddy currents, inductor model, on-chip inductors, quality factor, self resonance, substrate loss.

I. INTRODUCTION

THE lack of an accurate model for on-chip inductors presents one of the most challenging problem for silicon-based radio-frequency integrated circuits (RF IC's) designers. In conventional IC technologies, inductors are not considered as standard components like transistors, resistors, or capacitors, whose equivalent circuit models are usually included in the process description. However, this situation is rapidly changing as the demand for RF IC's continues to grow [1]–[5]. Various approaches for modeling inductors on silicon have been reported in past several years [6]–[12]. Most of these models are based on numerical techniques, curve fitting, or empirical formulae, and therefore are relatively inaccurate or not scalable over a wide range of layout dimensions and process parameters. For inductor design insights and optimization, a compact, physical model is required. The difficulty of physical modeling stems from the complexity of high-frequency phenomena such as the eddy current effect in the interconnect and the substrate loss in the silicon. The physical inductor model presented in this paper was first introduced in [13]. This paper reports in detail the development of the model.

II. INDUCTANCE AND RC PARASITICS OF A SPIRAL INDUCTOR

The key to accurate physical modeling is the ability to identify the relevant parasitics and their effects. Since an inductor is intended for storing magnetic energy only, the inevitable resistance and capacitance in a real inductor are counter-productive and thus are considered parasitics. The parasitic resistances dissipate energy through ohmic loss while the parasitic capacitances store electric energy. The physical model of a spiral inductor on silicon is shown in Fig. 1. The inductance and resistance of the spiral and underpass is represented by the se-
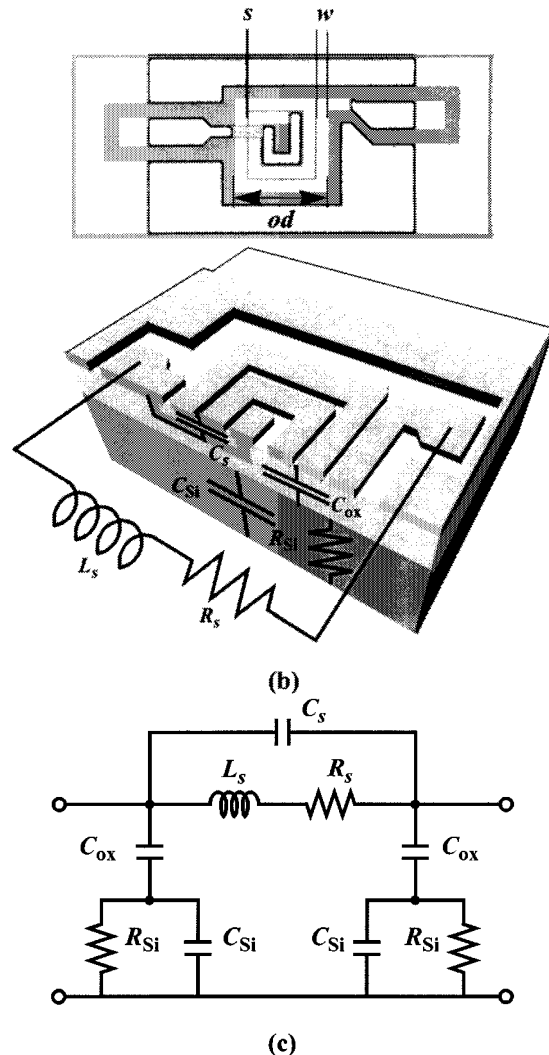
Fig. 1. Top(die photo); Middle, 3-D view; Bottom, the lumped physical model of a spiral inductor on silicon.

ries inductance, L_s, and the series resistance, R_s, respectively. The overlap between the spiral and the underpass allows direct capacitive coupling between the two terminals of the inductor. This feed-through path is modeled by the series capacitance, C_s. The oxide capacitance between the spiral and the silicon substrate is modeled by C_{ox}. The capacitance and resistance of the silicon substrate are modeled by C_{Si} and R_{Si}. The characteristics of each element are investigated extensively in the following sections.

A. Series Inductance

The foundation for computing inductance is built on the concepts of the self inductance of a wire and the mutual inductance between a pair of wires. A comprehensive collection of formulas
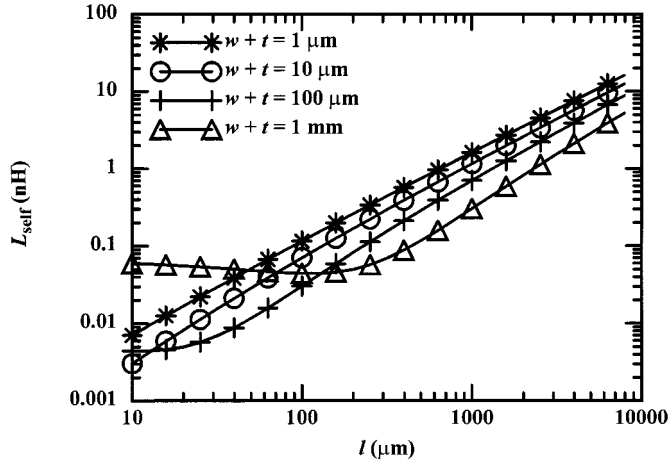
Fig. 2.   Dependency of self inductance on the wire cross-section dimensions for different wire lengths.

and tables for inductance calculation was summarized by Grover in [14].

The dc self inductance of a wire with a rectangular cross-section area can be expressed as follows:

$$L_{\text{self}} = 2l\left(\ln\frac{2l}{w+t} + 0.5 + \frac{w+t}{3l}\right) \qquad (1)$$

where

L_{self}	inductance in nH;
l	wire length in cm;
w	width in cm;
t	thickness in cm.

Since the inductance is primarily determined by the magnetic flux external to a wire, the variation in the wire cross-section dimensions has little effect on the inductance. In general, the wires with smaller cross-section area have a slightly larger inductance because they generate more magnetic flux external to the wire. It should also be pointed out that (1) is not valid for wires having cross-section dimension greater than approximately twice their length. While wires with such geometries are hardly used in practice, they point out the limitation of (1). Fig. 2 shows that the increase in inductance with length is slightly more than linear, which is due to the positive mutual coupling between parts of the wire. However, this transformer effect is insignificant as suggested by the logarithmic dependency on $(w + t)$ in (1). Typical wire segments of an on-chip spiral inductor have widths of 5–30 μm and lengths of 100–400 μm which result in self inductances of 0.7–1.1 nH/mm.

The mutual inductance between two parallel wires can be calculated using

$$M = 2lQ \qquad (2)$$

where M is the inductance in nH, l is the wire length in cm, and Q is the mutual inductance parameter, which can be computed with

$$Q = \ln\left[\frac{l}{GMD} + \sqrt{1 + \left(\frac{l}{GMD}\right)^2}\right]$$
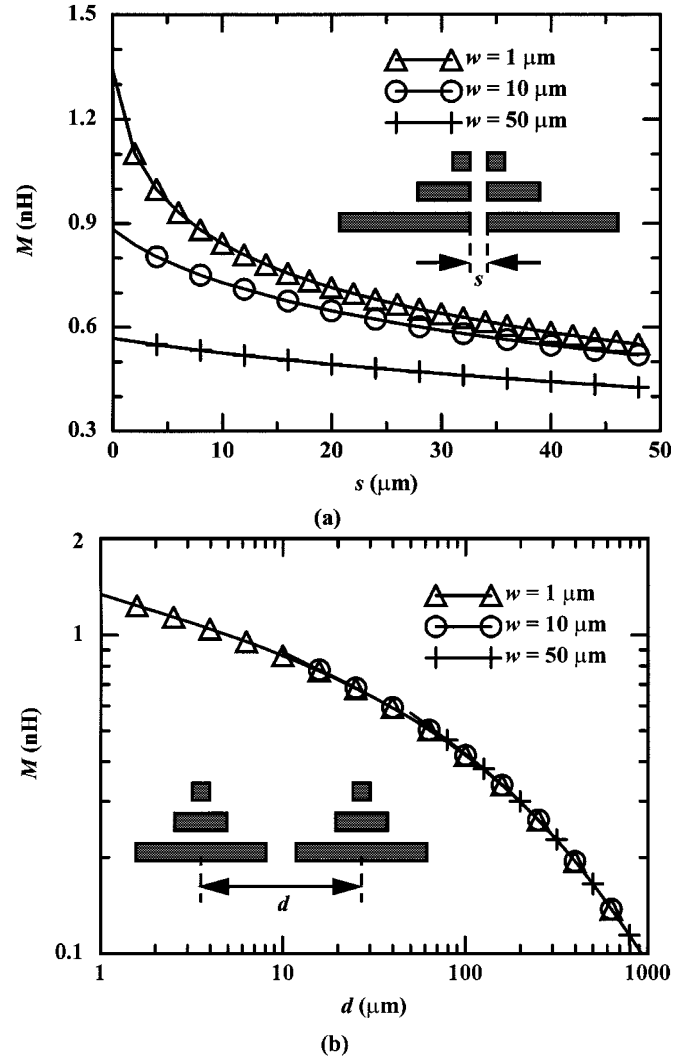$$- \sqrt{1 + \left(\frac{GMD}{l}\right)^2} + \frac{GMD}{l}. \qquad (3)$$

(a)

(b)

Fig. 3.   Mutual inductance and coupling coefficient between two wires as a function of (a) line-to-line spacing, s, and (b) line pitch, d.

In (3), GMD denotes the geometric mean distance between the wires, which is approximately equal to the pitch of the wires. A more precise expression for the GMD is given as

$$\ln GMD = \ln d - \frac{w^2}{12d^2} - \frac{w^4}{60d^4} - \frac{w^6}{168d^6}$$
$$- \frac{w^8}{360d^8} - \frac{w^{10}}{660d^{10}} - \cdots \qquad (4)$$

where w and d are the wire width and pitch in cm, respectively.

The self and mutual inductance are related as

$$M = k\sqrt{L_1 L_2} \qquad (5)$$

where L_1 and L_2 are the self inductance of the two wires. k is the mutual coupling coefficient. Fig. 3 shows the mutual inductance (M) as a function of the line-to-line spacing, s, and line pitch, d. The mutual inductance is larger for narrower space as the magnetic coupling is enhanced. The mutual inductance does not vary with the width when the pitch is fixed. This indicates that for on-chip inductors with the same turn-to-turn pitch, variations in spiral width have little effect on the overall inductance. This also implies that the variation of inductance due to metal etch variation is small.

Based on Grover's formulas, Greenhouse developed an algorithm for computingthe inductance of planar rectangular spirals [15]. The Greenhouse method states that the overall inductance of a spiral can be computed by summing the self inductance of each wire segment and the positive and negative mutual inductance between all possible wire segment pairs. The mutual inductance between two wires depends on their angle of intersection, length, and separation. Two wires orthogonal to each other have no mutual coupling since their magnetic flux are not linked together. The current flow directions in the wires determine the sign of coupling. The coupling is positive if the currents in the two wires are in same direction and negative for opposite currents. To evaluate the overall inductance of a N-turn square spiral, it involves $4N$ self-inductance terms, $2N(N-1)$ positive mutual-inductance terms and $2N^2$ negative mutual-inductance terms. Although various empirical formulas exist in literature for estimating spiral inductance [16]–[18], the Greenhouse method offers superior accuracy and therefore is used in our inductormodel.

B. Series Resistance

The current density in a wire is uniform at dc; however, as frequency increases, the current density becomes nonuniform due to the formation of eddy currents. The eddy current effect occurs when a conductor is subjected to time-varying magnetic fields and is governed by Faraday's law [19], [20]. Eddy currents manifest themselves as skin and proximity effects. In accordance with Lenz's law, eddy currents produce their own magnetic fields to oppose the original field. In the case of the skin effect, the time-varying magnetic field due to the current flow in a conductor induces eddy currents in the conductor itself. The proximity effect takes place when a conductor is under the influence of a time-varying field produced by a nearby conductor carrying a time-varying current. In this case, eddy currents are induced whether or not the first conductor carries current. This is essentially a transformer action. If the first conductor does carry a time-varying current, then the skin-effect eddy current and the proximity-effect eddy current superimpose to form the total eddy current distribution. Regardless of the induction mechanism, eddy currents reduce the net current flow in the conductor and hence increase the ac resistance. The distribution of eddy currents depends on the geometry of the conductor and its orientation with respect to the impinging time-varying magnetic field. The most critical parameter pertaining to eddy current effects is the skin depth which is defined as

$$\delta = \sqrt{\frac{\rho}{\pi\mu f}} \tag{6}$$

where ρ, μ, and f represent the resistivity in Ω-m, permeability in H/m, and frequency in Hz, respectively. The skin depth is also known as the "depth of penetration" since it describes the degree of penetration by the electric current and magnetic flux into the surface of a conductor at high frequencies. The severity of the eddy current effect is determined by the ratio of skin depth to the conductor thickness. The eddy current effect is negligible only if the depth of penetration is much greater than the conductor
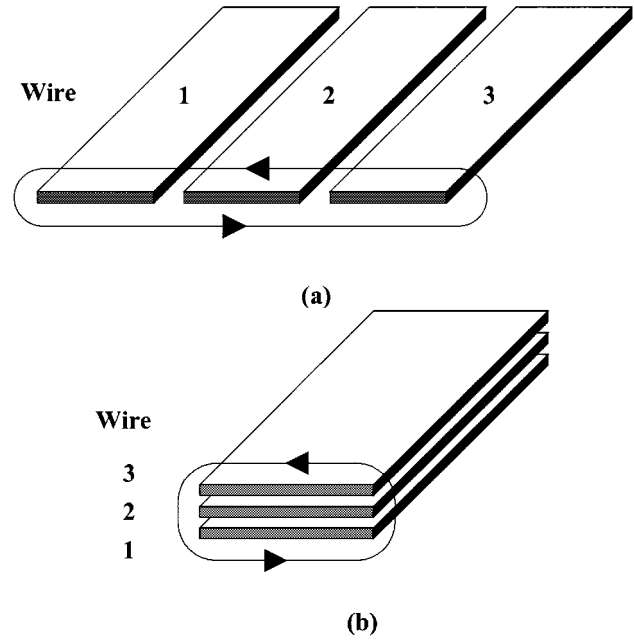

Fig. 4. Proximity effect on series resistance for (a) side-by-side and (b) stacked wires.

thickness. Since a spiral inductor is a multiconductor structure, eddy currents can potentially be caused by both proximity and skin effects. This section investigate the relative importance of the two effect.

Due to the close proximity between the conductor segments in a spiral inductor, the current in each segment can induce eddy currents in other segments and cause the resistance to increase. It is difficult to analytically determine the significance of the mutual eddy current and resistance caused by the proximity effect [19]. To investigate this problem, an electromagnetic field solver based on the finite element method [21] is employed to study the effect of magnetic mutual coupling on resistance. Three side-by-side wires, as shown in Fig. 4(a), are simulated. Each wire has a width and thickness of 20 μm and 1 μm, respectively. The spacing between lines is 2 μm. During the simulation, an ideal ground plane with infinite conductivity is placed 500 μm below the wires for carrying the return current. At 1 GHz, the simulated inductance and resistance matrix are

$$\begin{bmatrix} L_{11} & L_{12} & L_{13} \\ L_{21} & L_{22} & L_{23} \\ L_{31} & L_{32} & L_{33} \end{bmatrix} = \begin{bmatrix} 1.24 & 0.95 & 0.81 \\ 0.95 & 1.23 & 0.95 \\ 0.81 & 0.95 & 1.24 \end{bmatrix} \; \mu\text{H/m} \tag{7}$$

and

$$\begin{bmatrix} R_{11} & R_{12} & R_{13} \\ R_{21} & R_{22} & R_{23} \\ R_{31} & R_{32} & R_{33} \end{bmatrix} = \begin{bmatrix} 1961 & 15 & 0 \\ 15 & 2012 & 15 \\ 0 & 15 & 1961 \end{bmatrix} \; \Omega/\text{m} \tag{8}$$

respectively. L_{11}, L_{22}, and L_{33} are the self inductance of each wire and the off-diagonal terms represent the mutual inductances. The mutual coupling, k, between adjacent wires is 0.76 while k between wire 1 and wire 3 is 0.65. R_{11}, R_{22}, and R_{33} are the self resistances of each wire and the off-diagonal terms

represent the mutual resistances caused by proximity effect. The overall resistance of each wire can be obtained by summing the self and mutual resistances along a row or column of the resistance matrix. For instance, the resistance of wire 2 is 2042 Ω/m whereas for wire 1 and wire 3, it is 1976 Ω/m. The mutual resistance is less than 1% for side-by-side wires.

To investigate further the proximity effect on wire resistance, three stacked wires, as shown in Fig. 4(b), are simulated. The separation between wires is 1 μm. At 1 GHz, the inductance and resistance matrix are

$$\begin{bmatrix} L_{11} & L_{12} & L_{13} \\ L_{21} & L_{22} & L_{23} \\ L_{31} & L_{32} & L_{33} \end{bmatrix} = \begin{bmatrix} 1.24 & 1.23 & 1.21 \\ 0.21 & 1.24 & 1.23 \\ 1.21 & 1.23 & 1.24 \end{bmatrix} \quad \mu\text{H/m} \quad (9)$$

and

$$\begin{bmatrix} R_{11} & R_{12} & R_{13} \\ R_{21} & R_{22} & R_{23} \\ R_{31} & R_{32} & R_{33} \end{bmatrix} = \begin{bmatrix} 2004 & 498 & 489 \\ 498 & 2012 & 498 \\ 489 & 498 & 2004 \end{bmatrix} \quad \Omega\text{/m} \quad (10)$$

respectively. In this case, the magnetic coupling is nearly prefect ($k > 0.97$) and as a result, the mutually induced eddy current is more significant compared to the side-by-side configuration. In particular, the resistance of all three wires is approximately the same and is equal to 3000 Ω/m which is 50% greater than the self resistance of each wire.

Based on the foregoing analysis, the proximity effect between the turns of a spiral that are in the same plane can be neglected at 1 GHz. On the other hand, the proximity effect between stacked inductors must be included in the calculation of the series resistance of the spirals.

For on-chip spiral inductors, the line segments can be treated as microstrip transmission lines. In this case, the high frequency current recedes to the bottom surface of the wire, which is above the ground plane [22]–[24]. The attenuation of the current density (J in A/m²) as a function of distance (x) away from the bottom surface can be represented by the function

$$J = J_0 \cdot e^{-x/\delta}. \quad (11)$$

The current (I in A) is obtained by integrating J over the wire cross-sectional area. Since J only varies in the x direction, I can be calculated as

$$\begin{aligned} I &= \int J \cdot dA \\ &= \int_0^t J_0 \cdot e^{-x/\delta} \cdot w \cdot dx \\ &= J_0 \cdot w \cdot \delta \cdot (1 - e^{-t/\delta}) \end{aligned} \quad (12)$$

where t is the physical thickness of the wire. This last term in (12) can be defined as an effective thickness

$$t_{eff} = \delta \cdot (1 - e^{-t/\delta}). \quad (13)$$

At 1 GHz, the skin depth of Al and Cu is 2.8 μm and 2.5 μm, respectively. With $t = 3$ μm, t_{eff} of Al and Cu at 1 GHz is 1.8 μm and 1.7 μm, respectively.

The series resistance, R, can be expressed as

$$R = \frac{\rho \cdot l}{w \cdot t_{eff}} \quad (14)$$

where ρ and l represent the resistivity and length of the wire. As δ decreases with frequency, R increases. To compute the series resistance of a spiral inductor, l in (14) is set equal to the total length of all line segments.

C. Series Capacitance

The series capacitance (C_s) models the parasitic capacitive coupling between input and output ports of the inductor. This capacitance allows the signal to flow directly from the input to output port without passing through the spiral inductor. Based on the inductor's physical structure, both the crosstalk between adjacent turns and the overlap between the spiral and underpass contribute to C_s. However, since the adjacent turns are almost equipotential, the effect of the crosstalk capacitance is negligible. Furthermore, the crosstalk capacitance can be reduced by increasing the spacing between the turns. The effect of overlap capacitance is more significant because of the larger potential difference between the spiral and the underpass [25], [26]. Therefore, for most practical inductors, it is sufficient to model C_s as the sum of all overlap capacitances, which is equal to

$$C_s = n \cdot w^2 \cdot \frac{\epsilon_{\text{ox}}}{t_{\text{oxM1-M2}}} \quad (15)$$

where n is the number of overlap, w is the spiral line width, and $t_{\text{oxM1-M2}}$ is the oxide thickness between the spiral and the underpass.

D. Substrate Parasitics

The characteristics of microstrip structures on semiconductor substrate, especially metal on oxide on silicon, have been investigated extensively [27]–[30]. In general, a MOS microstrip structure can be modeled by a three-element network comprised of C_{ox}, R_{Si} and C_{Si} (see Fig. 1). C_{ox} represents the oxide capacitance whereas R_{Si} and C_{Si} represent the silicon substrate resistance and capacitance, respectively. The physical origin of R_{Si} is the silicon conductivity which is predominately determined by the majority carrier concentration. C_{Si} models the high-frequency capacitive effects occurring in the semiconductor. For spiral inductors on silicon, the lateral dimensions are typically a few hundred micro-meters which is much larger than the oxide thickness and is comparable to the silicon thickness. As a result, the substrate capacitance and resistance are approximately proportional to the area occupied by the inductor and can be estimated by

$$C_{\text{ox}} = \frac{1}{2} \cdot l \cdot w \cdot \frac{\epsilon_{\text{ox}}}{t_{\text{ox}}}, \quad (16)$$

$$C_{\text{Si}} = \frac{1}{2} \cdot l \cdot w \cdot C_{\text{sub}}, \quad (17)$$

and

$$R_{\text{Si}} = \frac{2}{l \cdot w \cdot G_{\text{sub}}} \quad (18)$$

where C_{sub} and G_{sub} are capacitance and conductance per unit area for the silicon substrates. ϵ_{ox} and t_{ox} denotes the dielectric constant and thickness of the oxide layer between the inductor and the substrate. The area of the spiral is equal to the product
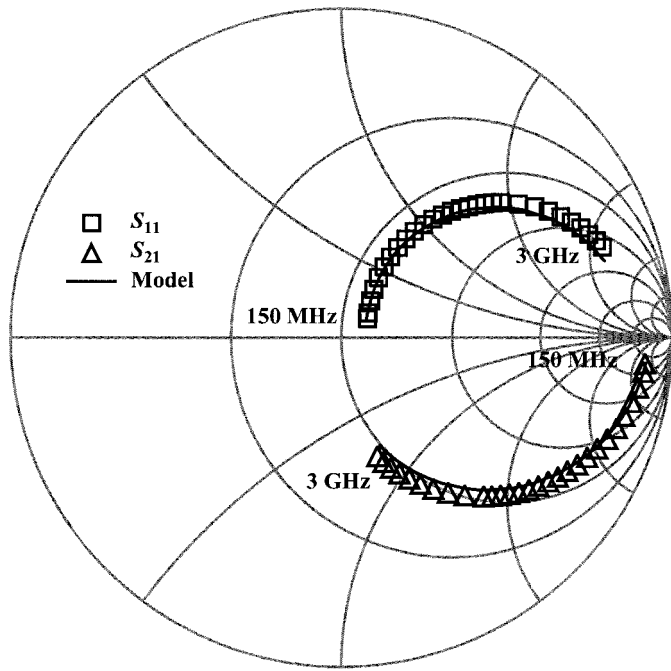
Fig. 5. Measured and modeled values of S_{11} and S_{21} from 150 MHz to 3 GHz plotted on a Smith chart.

Fig. 6. Effect of metal material on Q.

of the spiral length (l) and width (w). The factor of two in (16)–(18) accounts for the fact that the substrate parasitics are assumed to be distributed equally at the two ends of the inductor. C_{sub} and G_{sub} are functions of the substrate doping and are extracted from measurement results. For inductors fabricated in the same technology, C_{sub} and G_{sub} do not vary significantly. As a result, R_{Si} and C_{Si} only scales with l and w. The substrate type is another important factor for determining C_{sub} and G_{sub}. The current model is suitable only for uniformly doped substrates. For substrates with non-uniform doping profiles, additional parallel RC networks can be cascaded in series to predict the substrate behavior [30]. For inductors on epi substrates, the magnetic coupling between the spiral and the substrate can potentially induce eddy currents in the heavily doped silicon [12]. This effect is not accounted for in the current model. However, a recent study reveals that substrate eddy currents are insignificant even in epi substrates up to approximately 3 GHz [31].

III. EXPERIMENTAL RESULTS

To confirm that the physical model can indeed predict the overall inductor behavior, the measured and modeled two-port S-parameters of an inductor is shown in Fig. 5. The inductor is fabricated on 10 Ω-cm silicon with 4.5-μm oxide. The layout parameters include 7 turns, 13-μm width, 7-μm spacing, and 300-μm outer dimension. The spiral metal thickness is 1 μm with a measured dc sheet resistance of 30 m$\Omega/\square$. The two-port S parameters of the physical inductor model are generated using SPICE. The model components are computed using the algorithm and equations described in the previous section. The modeled results have been compared directly with the de-embedded S-parameters measured using an HP8720B network analyzer and coplanar probes. Excellent agreement is obtained [13].
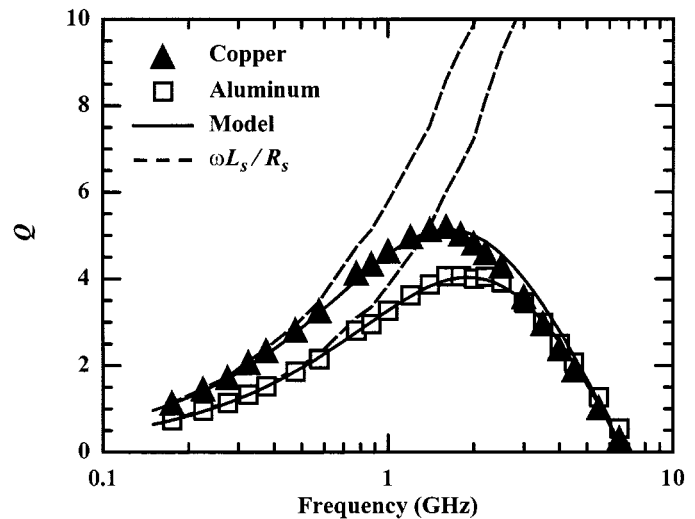
To demonstrate the scalability of our model, spiral inductors with various structural parameters including different metal material, metal thickness, oxide thickness, substrate material, and layout dimensions are fabricated and tested. Comparisons between the modeled and measured inductor quality factor, Q, are presented. The measurement and extraction techniques for Q has been reported [32].

Fig. 6 shows the measured and modeled Q of two inductors using copper and aluminum for the spiral. Both inductors have the same layout and use 1-μm thick metal. The measured dc sheet resistance of the copper and aluminum films is 20 m$\Omega/\square$ and 30 m$\Omega/\square$, respectively. At low frequencies, Q is well described by $\omega L_s/R_s$ for both inductors. The copper inductor has higher Q because it has lower series resistance. As frequency increases, the quality factors start to deviate from $\omega L_s/R_s$ due to the substrate effects. The rapid degradation of Q at high frequencies is a combined effect of the substrate loss and self-resonance. At high frequencies, the quality factors merge together and reduce to zero at the self-resonant frequency. This indicates that the substrate effects are independent of the metal layer. The close agreement between measured and modeled results indicates that the physical model is capable of accounting for variation in the metal material at rf.

Besides replacing aluminum by copper, another approach to reduce the series resistance is to use thicker metal for the spiral. Fig. 7 illustrates the effect of different metal thicknesses and schemes on Q. Four inductors with different metal thicknesses are fabricated and measured. A significant improvement in Q is obtained by increasing the aluminum thickness from 1 μm to 2 μm. However, the 3 μm data reveals that further thickening the metal has diminishing improvements in Q. This is due to the more severe skin effect suffered by the thicker spiral. Since the current flow is concentrated at the bottom of the spiral, metal thicker than the skin depth is ineffective for lowering the series resistance. For instance, at 1 GHz, the effective thicknesses of 1-μm, 2-μm, and 3-μm aluminum are 0.84 μm, 1.43 μm, and 1.83 μm, respectively. After including the substrate factors, the improvement in Q at 1 GHz is 57% and 81% as the metal

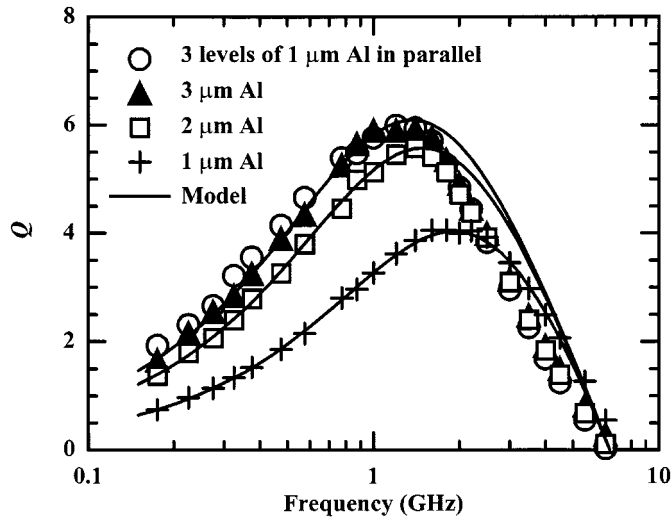Fig. 7.   Effect of metal scheme on Q.

Fig. 8.   Effect of oxide thickness on Q.

thickness is increased from 1 μm to 2μm and 3 μm. This effect is well predicted by the physical inductor model. Since the thinner metal suffers less severe skin effect, one may attempt to obtain more effective thickness by building an inductor with three levels of 1 μm aluminum connecting in parallel. The three spirals are connected to each other only at the two ends of the spiral and are isolated by oxide along the path. However, the mesaurement reveals that Q obtained in this case is the same as the one-level 3 μm inductor. This is attributed to the proxmity effect discussed earlier. Since the three layers are close to each other, there are almost perfect mutual coupling between them. As a result, the proximity effect induces additional eddy currents comparing to an isolated 1 μm layer. This explains that breaking up a single layer of 3-μm Al into three layers of 1-μm Al does not offer any improvement in Q. It should be pointed out that when thicker or multi-layer metals are used to implement the spiral, the crosstalk capacitance due to fringing fields may become significant and needs to be included in the modeling of the series capacitance (C_s) (see Section II). Nevertheless, this minor effect can be suppressed by increasing the separation betwen the spiral turns.

Q can also be improved by fabricating the inductor farther away the silicon substrate with thicker oxide. Three inductors with the same layout but different oxide thicknesses are fabricated and measured. Fig. 8 shows that increasing oxide thickness improves Q because the substrate effects are suppressed. But as frequency increases, C_{ox} is effectively short-circuited, substrate effects become dominant, and the Q's merge together.

Fig. 9 shows that lowering silicon substrate resistivity decreases R_{Si} and increases C_{Si}, causing the Q roll-off to occur at a lower frequency and a reduction of the self-resonance frequency. The increase in C_{Si} can be attributed to the fact that in a more conductive substrate, the electric field is terminated closer to the silicon surface and therefore the effective substrate thickness is thinner.

Fig. 10 illustrates the effect of layout area on Q for inductors with the same inductance but different layout parameters. Three 8-nH inductors are designed with outer dimension equal to 550, 400, and 300 μm. The inductors fabricated using larger area can
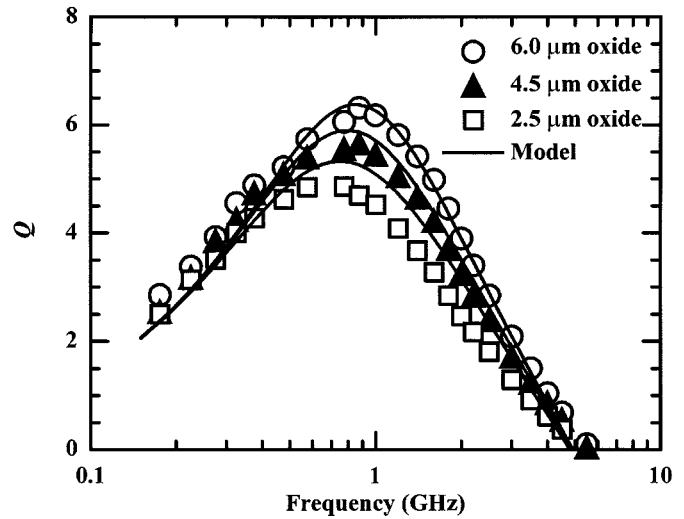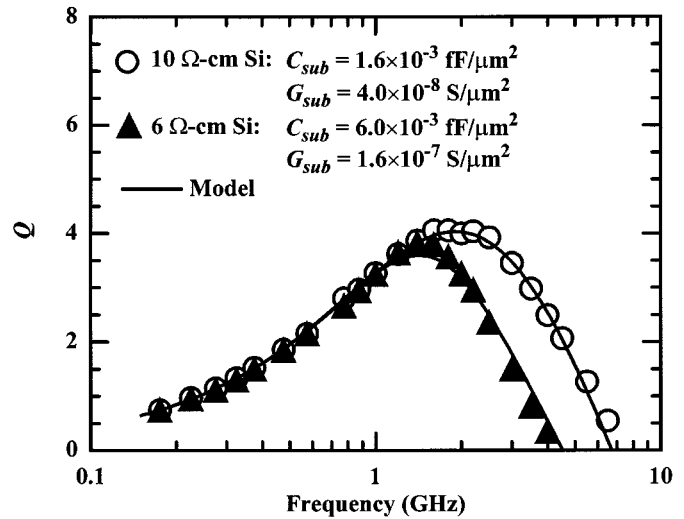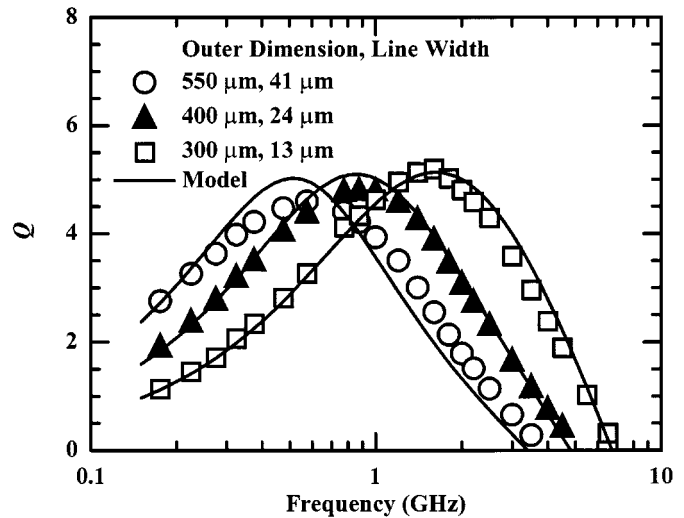

Fig. 9.   Effect of substrate resistivity on Q.

Fig. 10.   Effect of layout dimensions on Q.

accommodate wider line width; and as a result, achieve lower dc series resistance. However, they also have more shunt substrate
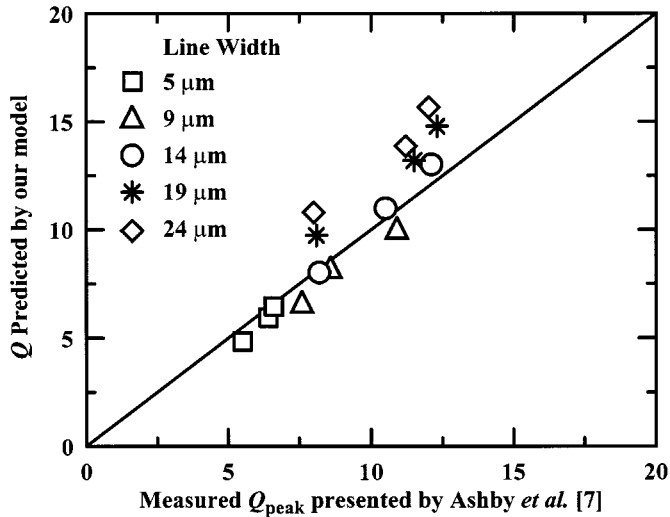
Fig. 11.   Verification of the physical model using published data.

parasitics because they occupy larger area. At low frequencies, the larger inductors offer higher Q's because of lower series resistance. At high frequencies, the substrate effects dominate and the smaller inductors actually achieve higher Q's. At about 1 GHz, the medium size inductor achieves highest Q because the resistive loss and the substrate effects are balanced.

Finally, published results are used to further confirm the inductor model and the equation for Q. Fig. 11 shows a comparison of the measured Q_{peak} of the inductors presented by Ashby et al. [7] and the Q values predicted by our model. These 15 inductors were fabricated using 4.5 μm of gold on silicon with high substrate sensitivity of about 200 Ω-cm. Good agreement is obtained. It is observed that there are approximately 20% deviations between the Q's predicted by our model and the measured values by Ashby et al. for 19 and 24 μm line width inductors. The model over estimated the inductor Q slightly since it neglects the proximity effects, which is more pronounced in spirals with wide line width. This observation indicates that for inductors with line width greater approximately 20 μm, the model must be improved to account for the proximity effects. However, the current model is sufficient for most practical inductors as the spiral sizes are usually limited by the chip area, which in turn prohibits the spiral line width to be greater than 20 μm.

IV. DESIGN METHODOLOGY

The trade-off between series resistance and substrate losses represents a practical scenario that RF designers encounter when using on-chp inductors in their circuits. As an example, consider that a 8-nH inductor is needed for an application at 1.6 GHz. Furthermore, because of the chip size limit, the inductor can occupy an area no larger than 400 μm by 400 μm. A design tool capable of optimizing the inductor layout by considering these constraints and the technology profile can significantly expedite the design flow. In Fig. 12, the Q contour plots are presented along with the measured Q values of a 8-nH $\{N = 7, w = 13 \ \mu$m, $s = 7 \ \mu$m, $od = 300 \ \mu$m$\}$ and a 2-nH $\{N = 3, w = 13 \ \mu$m, $s = 7 \ \mu$m, $od = 150 \ \mu$m$\}$ inductor at different frequencies. These plots are generated using the
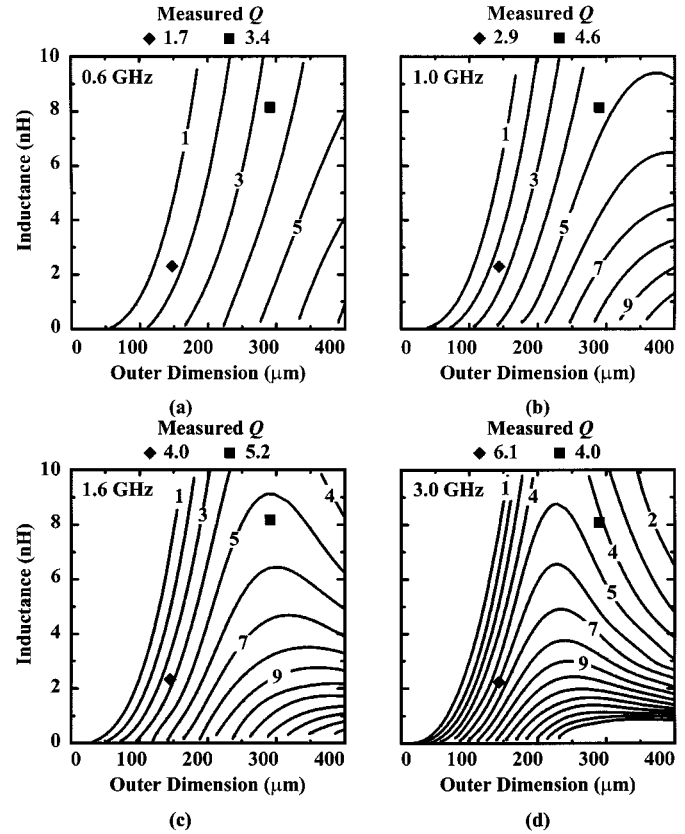

Fig. 12.   Contour plots of Q as a function of the inductance and outer dimension of square spiral inductors at (a) 0.6 GHz, (b) 1.0 GHz, (c) 1.6 GHz, and (d) 3.0 GHz.

physical inductor model. The contour curves represent the values of Q which are plotted as a function of the inductance and the outer dimension of the square spiral. Each point on the contour plot corresponds to a specific inductor layout design which is defined by the parameter set $\{N, w, s, od\}$, where N is the number of turns, w is the metal width, s is the metal spacing, and od is the outer dimension of the inductor [see Fig. 1(a)]. The contour plots can identify the optimal spiral layout for achieving a specific inductance with the highest Q possible for a given technology at a frequency of interest.

At low frequencies, such as 600 MHz shown in Fig. 12(a), larger areas result in higher Q's for all inductance values considered. This is because lower series resistances can be achieved and they are the limiting loss mechanism at low frequencies. As the frequency increases to 1 GHz, the substrate loss and self-resonance effects are starting to become important for inductors occupying large areas. As a result, the Q contours at the upper-right-hand corner begin to roll off. For the design example (maximum Q for a 8 nH inductor at 1.6 GHz), the contour plot in Fig. 12(c) shows that the highest Q achievable for 8 nH is 5.5 using this technology. This is achieved with a spiral that has an outer dimension of 300 μm. This is confirmed by the experimental data. Note that if the 8-nH inductor were fabricated using the maximum area available (i.e. 400 μm by 400 μm), a lower Q would result while precious chip area would be wasted. Fig. 12(d) shows that if the frequency of operation is increased to 3 GHz, the inductor with an outer dimension of 300 μm will no longer be the optimal design because the substrate effects are

now even more severe. In fact, an inductor layout that has an outer dimension of 220 μm will offer the highest Q of slightly above 5. In addition to optimizing Q in a limited area, the inductor design methodology presented above can have different combinations of optimization targets and constraints depending on the specific circuit applications.

V. CONCLUSIONS

In this paper, a physical model for planar spiral inductors on silicon is presented. The characteristics of each component in the model have been investigated extensively. The physical phenomena important to the prediction of Q are considered and analyzed. The scalable inductor model shows excellent agreement with measured data. The effects of various layout and process parameters on Q are explained using the inductor model and confirmed with experimental data.

ACKNOWLEDGMENT

REFERENCES

[1] B.-K. Kim et al., "Monolithic planar RF inductor and waveguide structures on silicon with performance comparable to those in GaAs MMIC," in *IEDM Tech. Dig.*, Dec. 1995, pp. 717–720.

[2] R. B. Merrill et al., "Optimization of high Q integrated inductors in multi-level metal CMOS," in *IEDM Tech. Dig.*, Dec. 1995, pp. 983–986.

[3] J. N. Burghartz, M. Soyuer, and K. A. Jenkins, "Integrated RF and microwave components in BiCMOS technology," *IEEE Trans. Electron Devices*, vol. 43, pp. 1559–1570, Sept. 1996.

[4] R. Groves, D. L. Harame, and D. Jadus, "Temperature dependence of Q and inductance in spiral inductors fabricated in a silicon-germanium/BiCMOS technololgy," *IEEE J. Solid-State Circuits*, vol. 32, pp. 1455–1459, Sept. 1997.

[5] M. Park et al., "High Q microwave inductors in CMOS double-metal technology," in *IEDM Tech. Dig.*, Dec. 1997, pp. 59–62.

[6] D. Lovelace, N. Camilleri, and G. Kannell, "Silicon MMIC inductor modeling for high volume, low cost applications," *Microw. J.*, pp. 60–71, Aug. 1994.

[7] K. B. Ashby et al., "High Q inductors for wireless applications in a complementary silicon bipolar process," *IEEE J. Solid-State Circuits*, vol. 31, pp. 4–9, Jan. 1996.

[8] J. Crols, P. Kinget, J. Craninckx, and M. S. J. Steyaert, "An analytical model of planar inductors on lowly doped silicon substrates for high frequency analog design up to 3 GHz," in *1996 Symp. VLSI Circuits Dig. Tech. Papers*, June 1996, pp. 28–29.

[9] J. R. Long and M. A. Copeland, "The modeling, characterization, and design of monolithic inductors for silicon RFIC's," *J. Solid-State Circuits*, vol. 32, pp. 357–369, Mar. 1997.

[10] A. M. Niknejad and R. G. Meyer, "Analysis and optimization of monolithic inductors and transformers for RF ICs," in *Proc. IEEE 1997 Custom Integrated Circuits Conf.*, May 1997, pp. 375–378.

[11] R. D. Lutz et al., "Modeling of spiral inductors on lossy substrates for RFIC applications," in *Proc. 1998 Radio Frequency Integrated Circuits Symp.*, June 1998, pp. 313–316.

[12] J. Lescot, J. Haidar, and F. Ndagijimana, "Accurate and fast modeling of planar inductors in CMOS technologies," in *Proc. 29th Eur. Solid State Device Research Conf.*, Sept. 1999.

[13] C. P. Yue et al., "A physical model for planar spiral inductors on silicon," in *IEDM Tech. Dig.*, Dec. 1996, pp. 155–158.

[14] F. W. Grover, *Inductance Calculations*. New York, NY: Van Nostrand, 1962.

[15] H. M. Greenhouse, "Design of planar rectangular microelectronic inductors," *IEEE Trans. Parts, Hybrids, Pack.*, vol. PHP-10, pp. 101–109, June 1974.

[16] F. E. Terman, *Radio Engineering Handbook*. New York: McGraw-Hill, 1943.

[17] P. Li, "PA new closed form formula for inductance calculation in microstrip line spiral inductor design," in *Electrical Performance of Electronic Packaging Conf. Dig.*, Dec. 1996, pp. 58–60.

[18] T. H. Lee, *The Design of CMOS Radio-Frequency Integrated Circuits*. Cambridge, U.K.: Cambridge Univ. Press, 1998.

[19] H. A. Wheeler, "Formulas for the skin effect," in *Proc. I. R. E.*, vol. 30, Sept. 1942, pp. 412–424.

[20] J. A. Tegopoulos and E. E. Kriezis, *Eddy Currents in Linear Conducting Media*. New York, NY: Elsevier, 1985.

[21] *Maxwell 2D Parameter Extractor User's Reference*: Ansoft Corp., 1997.

[22] R. A. Pucel, D. J. Massé, and C. P. Hartwig, "Losses in microstrip," *IEEE Trans. Microwave Theory Tech.*, vol. 16, pp. 342–350, June 1968.

[23] R. Faraji-Dana and Y. L. Chow, "The current distribution and ac resistance of a microstrip structure," *IEEE Trans. Microwave Theory Tech.*, vol. 38, pp. 1268–1277, Sept. 1990.

[24] Y. Eo and W. R. Eisenstadt, "High-speed VLSI interconnect modeling based on S-parameter measurements," *IEEE Trans. Comp., Hybrids, Manufact. Technol.*, vol. 16, pp. 555–562, Aug. 1993.

[25] R. H. Jansen et al., "Theoretical and experimental broadband characterization of multiturn square spiral inductors in sandwich type GaAs MMIC," in *Proc. 15th Eur. Microwave Conf.*, 1985, pp. 946–951.

[26] L. Wiemer and R. H. Jansen, "Determination of coupling capacitance of underpasses, air bridges and crossings in MICs and MMICs," *Electron. Lett.*, vol. 23, pp. 344–346, Mar. 1987.

[27] I. T. Ho and S. K. Mullick, "Analysis of transmission lines on integrated-circuit chips," *IEEE J. Solid-State Circuits*, vol. SC-2, pp. 201–208, Dec. 1967.

[28] H. Hasegawa, M. Furukawa, and H. Yanai, "Properties of microstrip line on Si-SiO$_2$ system," *IEEE Trans. Microwave Theory Tech.*, vol. MTT-19, pp. 869–881, Nov. 1971.

[29] G. W. Hughes and R. M. White, "Microwave properties of nonlinear MIS and Schottky-barrier microstrip," *IEEE Trans. Electron Devices*, vol. ED-22, pp. 945–955, Oct. 1975.

[30] J.-S. Yuan, W. R. Eisenstadt, and J. J. Liou, "A novel lossy and dispersive interconnect model for integrated circuit simulation," *IEEE Trans. Comp., Hybrids, Manufact. Technol.*, vol. 13, pp. 275–280, June 1990.

[31] C. P. Yue and S. S. Wong, "A study on substrate effects of silicon-based RF passive components," in *1999 IEEE MTT-S Int. Microwave Symp. Dig.*, June 1999, pp. 1625–1628.

[32] ——, "On-chip spiral inductors with patterned ground shields for Si-based RF IC's," *IEEE J. Solid-State Circuits*, vol. 33, pp. 743–752, May 1998.

C. Patrick Yue (S'93–M'99) received the B.S. degree in electrical engineering (with highest honors) from the University of Texas at Austin in 1992 and the M.S and Ph.D. degrees in electrical engineering from Stanford University, Stanford, CA, in 1994 and 1998, respectively. His doctoral dissertation at Stanford focused on the integration of spiral inductors for silicon RFIC's.

He has held summer positions at Texas Instruments, Dallas, TX, and Hewlett Packard Laboratories, Palo Alto, CA, in 1993 and 1994, respectively. From August to November 1998, he was a Research Associate at the Center for Integrated Systems, Stanford, CA, where he conducted research on high-frequency modeling of on-chip passive components and interconnects. In December 1998, he co-founded T-Span Systems Corp., Palo Alto, where he is involved in RF IC design and device modeling for wireless LAN applications. He has authored or co-authored more than 15 technical articles and has contributed to *The VLSI Handbook* (Piscataway, NJ: IEEE Press, 1999).

Dr. Yue is a member of Tau Beta Pi.

S. Simon Wong (S'77–M'83–SM'91–F'99) received the B.E.E. and B.M.E. degrees from the University of Minnesota, Minneapolis, in 1975 and 1976, respectively, and the M.S. and Ph.D. degrees from the University of California, Berkeley, in 1978 and 1983, respectively.

From 1978 to 1980, he was with National Semiconductor Corporation, designing MOS dynamic memories. From 1980 to 1985, he was with Hewlett-Packard Laboratories, Palo Alto, CA, working on advanced MOS technologies. From 1985 to 1988, he was an Assistant Professor in the School of Electrical Engineering, Cornell University, Ithaca, NY.. In 1988, he joined Stanford University, Stanford, CA, where he is now Professor of electrical engineering. His research interests include high performance device structures, advanced interconnection technologies, and multichip modules. Current research concentrates on interconnect technologies and high-frequency modeling of interconnect network.